

Global existence for chemotaxis with finite sampling radius

*Original*

Global existence for chemotaxis with finite sampling radius / Hillen, T.; Painter, K.; Schmeiser, C.. - In: DISCRETE AND CONTINUOUS DYNAMICAL SYSTEMS. SERIES B.. - ISSN 1531-3492. - 7:1(2007), pp. 125-144.  
[10.3934/dcdsb.2007.7.125]

*Availability:*

This version is available at: 11583/2974230 since: 2022-12-29T15:47:19Z

*Publisher:*

American Institute of Mathematical Sciences

*Published*

DOI:10.3934/dcdsb.2007.7.125

*Terms of use:*

This article is made available under terms and conditions as specified in the corresponding bibliographic description in the repository

*Publisher copyright*

(Article begins on next page)

# Global Existence for Chemotaxis with Finite Sampling Radius

T. Hillen<sup>\*</sup>      K. Painter<sup>†</sup>      C. Schmeiser<sup>‡</sup>

February 3, 2006

**Abstract:** Migrating cells measure the external environment through receptor-binding of specific chemicals at their outer cell membrane. In this paper we incorporate this non-local sampling into a chemotactic model. We prove that, in contrast to the classical chemotaxis model, the non-local model has globally existing solutions for any space dimension. We use a classification of spikes and plateaus and show that steady state solutions cannot be of spike-type. Finally, we use numerical simulations to support the theoretical results, illustrate the ability of the model to give rise to pattern formation and consider some biologically relevant extensions of the model.

**Keywords:** Chemotaxis, non-local gradient, global existence, pattern formation

## 1 Introduction

Chemotaxis, the active orientation of cells and organisms along chemical gradients, plays a crucial role in many biological processes, including embryonic development, immunology and cancer growth. Accordingly, a vast amount of research, both experimental and theoretical, has been devoted to understanding the mechanistic basis of chemotaxis.

---

<sup>\*</sup>University of Alberta, Edmonton T6G2G1, Canada, thillen@ualberta.ca, supported by NSERC

<sup>†</sup>Heriot-Watt University, Edinburgh, EH11 1UF, UK, painter@ma.hw.ac.uk, partially supported by NIH...

<sup>‡</sup>

In 1953, Patlak [32] introduced the first mathematical model for chemotaxis. A similar model was derived by Keller and Segel in 1970 [17], albeit under different assumptions. These pioneering works have initiated an intensive mathematical investigation of the Patlak-Keller-Segel (PKS) model over the last 30 years. Of particular interest is the following special case, which we refer to as the *classical chemotaxis model*:

$$\begin{aligned} u_t &= \nabla \cdot (\nabla u - \chi u \nabla s) \\ s_t &= D_s \Delta s + \alpha u - \beta s. \end{aligned} \tag{1}$$

The function  $u(x, t)$  denotes the population density at time  $t$  and location  $x$ , while  $s(x, t)$  denotes the concentration of a chemical signal; in the above model this is produced by the species themselves. The parameters  $\chi, \alpha, \beta, D_s$  are non-negative. The system (1) has been studied on bounded domains with appropriate boundary conditions (Neumann, Dirichlet, Robin etc.) or on unbounded domains. An important feature of the above model lies in its ability to exhibit pattern formation, or “aggregation”: an example of a typical aggregation pattern for (1) can be found in Figure 4 (a). As such, models based on the above equations have been applied to a wide range of biological pattern formation processes, including mound formation in the slime mold *Dictyostelium*, bacterial pattern formation, animal pigmentation patterns and limb bud patterning ([17, 38, 30, 21]).

In this paper we study a simple modification of the classical chemotaxis model (1), where the gradient sensing term  $\nabla s$  is replaced by the non-local gradient  $\overset{\circ}{\nabla}_\rho s$ :

$$\begin{aligned} u_t &= \nabla \cdot (\nabla u - \chi u \overset{\circ}{\nabla}_\rho s) \\ s_t &= D_s \Delta s + \alpha u - \beta s, \end{aligned} \tag{2}$$

where for  $\rho > 0$  the non-local gradient, which was introduced in [25], is defined as

$$\overset{\circ}{\nabla}_\rho s(x, t) = \frac{n}{\omega \rho} \int_{S^{n-1}} \sigma s(x + \rho \sigma, t) d\sigma, \tag{3}$$

where  $\omega = |S^{n-1}|$  and  $S^{n-1}$  denotes the  $(n - 1)$ -dimensional unit sphere in  $\mathbb{R}^n$ . The nonlocal gradient describes sensing of the chemical signal over an effective sampling radius  $\rho > 0$ .

As we shall demonstrate, the modified model, while still capable of giving rise to the fundamental pattern formation behaviour, overcomes certain shortcomings of the classical chemotaxis model — namely the global in time existence and boundedness of solutions of (2) for  $\rho > 0$  in any space dimension as well as that patterns are of plateau-type. Details behind this model

and about the analysis will be given later. First we summarise some results of the classical chemotaxis model (1) relevant to the analysis here.

For (1) on bounded domains it has been shown that the qualitative behaviour of solutions depend strongly on the space dimension. An extensive review article by D. Horstmann, [14], concerning (1) and related models provides greater detail, here we summarise the essentials. In one space dimension, solutions exist globally, a fact only recently proven ([24]). In Hillen and Potapov [12] numerical and asymptotic arguments have been applied to demonstrate solutions to (1) in one-dimension typically form spikes. For two-dimensional domains, global existence depends on a threshold: when the initial mass lies below the threshold solutions exist globally, while above the threshold solutions blow up in finite time (see references in Horstmann [14] or in Hillen and Painter [11], and [7] for a recent result). Under the biologically relevant cases for aggregation to occur, the initial conditions typically lie above this threshold — hence while the model does predict aggregation, this takes the form of a finite time blow-up.

While the early evolution of solutions to (1) may be a reasonable accurate description for the initial aggregation of microorganisms and cells, blow-up is undesirable from a modelling perspective — formation of a singularity is clearly biologically unrealistic. Chemotacting bacteria such as *Salmonella typhimurium* or slime molds such as *Dictyostelium* tend to aggregate in finite size swarms. Further, the blow-up behaviour of the model prevents modelling post-aggregation stages: for example, during the formation of a fruiting body in *Dictyostelium*, a number of distinct stages take place following the initial aggregation of the cells, including the differentiation and sorting into pre-stalk and pre-spore cells and formation of a “slug” (e.g. see [40]). Hence, system (1) can only be considered valid up to a certain time point, after which further modelling assumptions must be considered. In the literature (at least) four mechanisms have been identified which can prevent blow-up: (i) saturation effects, (ii) volume filling, (iii) attraction-repulsion mechanisms, (iv) finite sampling radius.

All of the above mechanisms, based on biologically realistic considerations, can alter the above equations (1) such that solutions exist globally. Hence we call them *regularizations*. While (i), (ii), (iii) have been studied in the literature, the aim of this paper is to study (iv) in detail.

As seen for the classical chemotaxis model (1), typical non-trivial solutions form very sharp and thin local maxima (spikes). These spikes remain bounded in 1-D and blow up in  $n$ -D,  $n \geq 2$ . For the volume filling model typical patterns are of plateau-type (see Painter and Hillen [28], Dolak and Schmeiser [6]). In Hillen [9] a classification of spikes versus plateaus is given,

using the non-local gradient (3). We show in this paper that solutions of (2) are global in time and steady states are of plateau-type. We prove that the non-local chemotaxis model (2) cannot have spike steady states.

The paper is organized as follows. In section 2 we derive finite sampling radius from biological observations. We properly define the nonlocal gradient and we show some basic properties of  $\overset{\circ}{\nabla}_\rho$ . In section 3 we prove global in time existence of solutions to the model (2) in any space dimension. The proof relies on the trace theorem for the nonlocal gradient and the Nash estimate. In section 4 we employ linear stability analysis to determine the conditions under which aggregation is possible, we summarise the classification into spikes and plateaus from [9], and we show that (2) cannot have spike steady states. Moreover, we construct approximate plateau steady states. In section 5 we present numerical simulations for the non-local model (2), illustrate the possibility of pattern formation and the dependence on the sampling radius  $\rho > 0$ . In particular, we show that as  $\rho \rightarrow 0$  the solutions become singular (blowup). We close the paper with a discussion section 6, where we compare our findings to the known results of the three previously studied regularizations (i)-(iii). In addition we give an outlook to future research directions.

## 2 The Finite Sampling Radius

While details vary between systems, common to all processes of chemosensitive movement is the detection and response to an external signal. In cells, detection of the external chemoattractant typically occurs through binding to specific membrane receptors, for example Rappel et al. [34] demonstrate that cells polarise in a signal gradient by measuring the actual signal concentration along their body membrane. Incorporating the “sampling radius” into models for chemotaxis thus arises naturally from these considerations: at its most intuitive level it could represent the movement response through signal detection at the cell membrane. In practice, this sampling radius may be many times larger than the physical extent of the cell: studies on the physics of chemoreception by Purcell and Berg [2] indicate that the *effective* sampling volume depends on the time taken for a signal to be processed by a cell, and for realistic parameter values in *Dictyostelium* this can swell the physical sampling volume by several times [26]. The actual sampling volume can also be affected by cell shape: migrating cells extend a variety of cellular protrusions, including pseudopodia, lamellipodia and filopodia,

the latter extending up to 80-100  $\mu\text{m}$  in length.

Such considerations led Othmer and Hillen [25] to propose the inclusion of a finite sampling radius in a model, as defined in (3). In this section we demonstrate how such models can be derived from two different approaches: the first, a phenomenological approach, considers its derivation from a force balance approach, while the latter considers the derivation directly from the kinetic transport equation.

## 2.1 Derivation from Force Balance

Our phenomenological derivation for a class of non-local models including 2 follows the approach in [31]. Macroscopic movement equations derive from Newton's law by considering the forces exerted by a cell in multiple directions. We assume that the cell density,  $u(\mathbf{x}, t)$  follows the general conservation law

$$u_t = -\nabla \cdot \mathbf{J} + g(\cdot)$$

where  $g(\cdot)$  represents cell kinetics and  $\mathbf{J}$  describes the cell flux. Herein we assume kinetics are negligible on the timescale of movement ( $g(\cdot) = 0$ ). We assume the flux comprises of both a diffusive component, modelling random effects, and a guided component modelling the chemotactic response,

$$\mathbf{J} = \mathbf{J}_{\text{diffusion}} + \mathbf{J}_{\text{chemotaxis}}$$

where we take  $\mathbf{J}_{\text{diffusion}} = -D\nabla u$  for simplicity. Following the approach of [31] we propose the chemotactic flux takes the form

$$\mathbf{J}_{\text{chemotaxis}} = u\phi\mathbf{F}$$

where  $\phi\mathbf{F}$  represents the *chemotactic velocity* with motility coefficient  $\phi$  (which could incorporate effects due to other chemicals, ECM or cell interactions) and  $\mathbf{F}$  is the net force generated by the cell in response to the chemical environment. The above follows directly from Newton's law, assuming negligible inertia (reasonable at the low speeds of cell migration) and that drag is proportional to velocity.

The mechanism for force generation varies greatly between cells. In amoeboidal cells such as *Dictyostelium* and leukocytes, force is generated through the creation of adhesive attachments at the cell membrane with the substrate/ECM; such cells frequently extend pseudopods in multiple directions during movement, e.g. Varnum-Finney *et al.* [39]. Under this assumption, a one-dimensional cell centred at  $x$  and of radius  $\rho$  can generate

forces in the positive/negative direction of magnitude  $f^\pm \equiv f(a(x \pm \rho))$ , where  $a$  represents the number of adhesive attachments made by the cell. The net force is

$$F = f(a(x + \rho)) - f(a(x - \rho)).$$

which, upon substituting into the flux gives,

$$J = -D_u u_x + u\phi(f(s(x + \rho)) - f(s(x - \rho))).$$

Our mass conservation thus takes the form of the non-local PDE

$$u_t = D_u u_{xx} - (u\phi(f(a(x + \rho)) - f(a(x - \rho))))_x.$$

The extension into higher dimensions is similar. The magnitude of the force in a direction  $\nu$  will depend on the number of attachments made at the boundary in that direction,

$$f(\nu) = f(a(\mathbf{x} + \nu\rho)).$$

Summing over all directions to obtain the net force, substituting into the conservation equation we obtain a non-local model for cell movement:

$$u_t = D_u \Delta u - \nabla \cdot \left( u\phi \int_{S^{n-1}} \nu f(a(\mathbf{x} + \nu\rho)) d\nu \right).$$

where  $\nu$  now represents the outer-unit norm and  $S^{n-1}$  the surface of the unit  $n$ -sphere.

To apply the model to chemotactic-cell movement, we must consider the generation of force in response to an external signal. Here, in the interests of model simplicity, we ignore many of the details; a comprehensive model could incorporate any number of processes, including binding of chemoattractant to cell surface receptors, internal signalling, *etc.* We take the simplest assumption: the number of focal attachments, and hence the force, generated along the membrane is directly proportional to the local chemoattractant concentration, i.e.

$$f(a(\mathbf{x} + \nu\rho)) \propto b(\mathbf{x} + \nu\rho) \tag{4}$$

where  $b$  represents the concentration of attractant-bound receptors. Under the simple model for attractant-receptor binding (Section 6.1), we assume

$$b = \frac{Ks}{\gamma + s} \tag{5}$$

Clearly, for sufficiently large  $\gamma$ , we can take  $b \propto s$ , leading to the non-local model

$$\begin{aligned} u_t &= D_u \Delta u - \nabla \cdot \left( u \phi \int_{S^{n-1}} \nu s(\mathbf{x} + \nu \rho) d\nu \right), \\ s_t &= D_s \Delta s + h(u, s). \end{aligned}$$

With the scaling  $\phi = \frac{n}{\omega \rho}$ , we obtain the nonlocal system (2)-(3). This scaling is chosen to permit direct comparison with the classical chemotaxis system (1).

## 2.2 Derivation from a Kinetic Transport Equation

The nonlocal model can also be derived from a kinetic transport model, in which cells are assumed to perform a velocity jump process. The nondimensionalized master equation then has the form

$$\varepsilon^2 f_t + \varepsilon v \cdot \nabla f = T_0(f) + \varepsilon T_1(f),$$

where  $f(x, v, t)$  is the distribution function of cells in the position-velocity phase space, and the small dimensionless parameter  $\varepsilon$  results from a macroscopic diffusion scaling. The left hand side of the equation models movement with constant velocities, whereas the right hand side describes the velocity jumps. We consider a dominating isotropic process, where all possible post-jump velocities have the same probability:

$$T_0(f)(x, v, t) = \frac{1}{|V|} u_f(x, t) - f(x, v, t) = \frac{1}{|V|} \int_V [f(x, v', t) - f(x, v, t)] dv'.$$

Here  $V$  and  $|V|$  denote the set of all possible velocities (assumed to be rotationally symmetric) and its measure, respectively. This is the simplest possible model. For the second process, the cell measures the chemical concentration along a sphere with radius  $\rho$  around its position  $x$ . Post-jump velocities with directions of higher chemical concentration occur with higher probability. The turning operator is given by

$$T_1(f)(x, v, t) = \int_V \left[ \phi \left( s \left( x + \rho \frac{v}{|v|}, t \right) \right) f(x, v', t) - \phi \left( s \left( x + \rho \frac{v'}{|v'|}, t \right) \right) f(x, v, t) \right] dv',$$

where the rate  $\phi(s(x + \rho v'/|v'|, t))$  ( $\phi$  increasing) of jumping from velocity  $v$  to  $v'$  could be modelled as proportional to the concentration of bound receptors as a function of the extracellular signal  $s$ . A continuum model of



Keller-Segel type can be derived by the macroscopic limit  $\varepsilon \rightarrow 0$ . We shall sketch the formal procedure. More details and rigorous justifications can be found in [10], [25], [4].

Obviously, the limiting distribution function is independent from the velocity:  $f_0(x, v, t) = u(x, t)/|V|$  with the macroscopic cell density  $u$ , which is not determined by the limiting equation  $T_0(f_0) = 0$ . After dividing the transport equation by  $\varepsilon$ , we have

$$\varepsilon f_t + v \cdot \nabla f = T_0 \left( \frac{f - f_0}{\varepsilon} \right) + T_1(f).$$

Denoting the limit of  $(f - f_0)/\varepsilon$  by  $R$ , we obtain

$$R = -v \cdot \nabla f_0 + T_1(f_0) + u_1$$

Finally, division of the transport equation by  $\varepsilon^2$  and integration with respect to  $v$  gives the conservation equation

$$(u_f)_t + \nabla \cdot \int_V v \frac{f - f_0}{\varepsilon} dv = 0.$$

In the limit  $\varepsilon \rightarrow 0$ , the convection-diffusion equation

$$u_t + \nabla \cdot (-D \nabla u + u v_s) = 0,$$

is obtained. The diffusivity is given by  $D = |V|^{-1} \int_V v \otimes v dv$ , and the macroscopic chemotactic velocity can be computed as

$$v_s = \chi \int_{S^{n-1}} \sigma \phi(s(x + \rho \sigma, t)) d\sigma, \quad (6)$$

where the constant  $\chi$  results from the integral in the radial direction. For linear  $\phi$ , the chemotactic velocity is proportional to the nonlocal approximation of the gradient as in (2). In Section 5, numerical experiments are also carried out with a nonlinear  $\phi$ , modelling saturation of bound receptors.

### 3 The Nonlocal Chemotaxis Model Prevents Blow-up

The main theoretical result of this paper is global existence and uniform boundedness of solutions of (2) subject to the initial conditions

$$u(x, 0) = u_I(x), \quad s(x, 0) = s_I(x). \quad (7)$$

Let  $\|\cdot\|_p$  denote the  $L^p(\mathbb{R}^n)$ -norm.

We start with a general lemma on convection-diffusion equations.

**Lemma 3.1** *Let the components of the vector field  $v : \mathbb{R}^n \times (0, \infty) \rightarrow \mathbb{R}^n$  be uniformly bounded, and let  $u_I \in L^\infty(\mathbb{R}^n) \cap L^1(\mathbb{R}^n)$  satisfy  $u_I \geq 0$ . Then the solution of the initial value problem*

$$u_t = \nabla \cdot (\nabla u - uv), \quad u(x, 0) = u_I(x),$$

*satisfies  $u \in L^\infty((0, \infty) \times \mathbb{R}^n)$  and*

$$\sup_t \|u\|_\infty \leq C(\|u_I\|_1, \|u_I\|_\infty, \sup_t \|v\|_\infty, n).$$

**Proof:** We start with a formal computation. For  $1 \leq p < \infty$ , we obtain

$$\begin{aligned} \frac{d}{dt} \|u\|_p^p &= 2(p-1) \left( -\frac{2}{p} \|\nabla(u^{p/2})\|_2^2 + \int_{\mathbb{R}^n} u^{p/2} v \cdot \nabla(u^{p/2}) dx \right) \\ &\leq 2(p-1) \left( -\frac{1}{p} \|\nabla(u^{p/2})\|_2^2 + \frac{p}{4} \sup_t \|v\|_\infty^2 \|u\|_p^p \right). \end{aligned} \quad (8)$$

Now, similarly to [1] we use the Nash inequality [23]

$$\|f\|_2^{1+2/n} \leq c_n \|f\|_1^{2/n} \|\nabla f\|_2,$$

with  $f = u^{p/2}$  and with the abbreviation  $z_p(t) = \|u(\cdot, t)\|_p^p$ :

$$\frac{dz_p}{dt} \leq 2(p-1)z_p \left( \frac{p}{4} \sup_t \|v\|_\infty^2 - \frac{z_p^{2/n}}{pc_n^2 z_{p/2}^{4/n}} \right). \quad (9)$$

This will lead to a global-in-time bound for  $z_p$  in terms of a bound for  $z_{p/2}$ . The strategy of the rest of the proof is to iteratively obtain bounds for  $z_{2^k}$  for all  $k \in \mathbb{N}$  and to show that these bounds are uniform in  $k$  such that the result of the lemma follows by  $k \rightarrow \infty$ .

By interpolation, we have that

$$\|u_I\|_p \leq \|u_I\|_\infty^{(p-1)/p} \|u_I\|_1^{1/p} \leq \max\{\|u_I\|_\infty, \|u_I\|_1\} =: K.$$

We use induction to show that

$$z_{2^k}(t) \leq M_k, \quad (10)$$

where

$$M_k = \max\{K^{2^k}, A2^{nk} M_{k-1}^2\}, \quad M_0 = K,$$

and a  $k$ -independent constant

$$A := 2^{-n}(\sup_t \|v\|_\infty c_n)^n.$$

Indeed, for  $k = 0$  we use  $z_1 \leq K$  (as a consequence of conservation of mass) and obtain from (9) that

$$\frac{dz_2}{dt} \leq 2z_2 \left( \frac{1}{2} \sup_t \|v\|_\infty^2 - \frac{z_2^{2/n}}{2c_n^2 K^{4/n}} \right). \quad (11)$$

The right hand side of (11) has two zeroes, at  $z_2 = 0$  and  $z_2 = 2^n AK^2$ . If the initial condition  $z_2(0) \geq 2^n AK^2$  then  $z_2(t) \leq z_2(0) = \|u(\cdot, 0)\|_2^2 \leq K^2$ . If  $z_2(0) \leq 2^n AK^2$  then  $z_2(t) \leq 2^n AK^2$ . Which proves the claim (10) for  $k = 1$ .

Now assume (10) holds for  $k - 1$ . Then

$$\frac{dz_{2^k}}{dt} \leq 2(2^k - 1)z_{2^k} \left( \frac{2^k}{4} \sup_t \|v\|_\infty^2 - \frac{z_{2^k}^{2/n}}{2^k c_n^2 M_{k-1}^{4/n}} \right). \quad (12)$$

The zeroes of the right hand side (12) are now 0 and  $A2^{nk}M_{k-1}^2$ . With the same argument as above we conclude that

$$z_{2^k}(t) \leq \max\{K^{2^k}, A2^{nk}M_{k-1}^2\}$$

which proves the claim (10).

Again by induction it is straightforward to show that

$$K^{2^k} \leq 2^{kn} M_{k-1}^2,$$

Hence with  $B = \max\{A, 1\}$ , we may change the definition of the upper bounds to

$$M_k = B2^{kn} M_{k-1}^2, \quad M_0 = K.$$

The solution of this recursion is

$$M_k = B^{2^k-1} 2^{a_k n} K^{2^k},$$

with  $a_k = k + 2a_{k-1}$ ,  $a_0 = 0$ . Since  $a_k = 2^{k+1} - k - 2 < 2^{k+1}$  and  $B \geq 1$ , we obtain  $M_k \leq (B4^n K)^{2^k}$  and, thus, the uniform-in- $k$  bound

$$\sup_t \|u\|_{2^k} \leq 4^n \max\{\|u_I\|_\infty, \|u_I\|_1\} \max\left\{1, 2^{-n}(\sup_t \|v\|_\infty c_n)^n\right\},$$

completing the proof. ■

**Theorem 3.1** *Let  $\chi, \rho, D_s, \alpha$ , and  $\beta$  be positive constants and let the initial data satisfy*

$$u_I \in L^\infty(\mathbb{R}^n) \cap L^1(\mathbb{R}^n), \quad s_I \in W^{1,q}(\mathbb{R}^n),$$

*with  $1 < q < \frac{n}{n-1}$ . Then (2), (7) has a global solution with*

$$u \in L^\infty((0, \infty) \times \mathbb{R}^n),$$

*i.e., the cell density is uniformly bounded in position and time.*

**Remark 1** *Almost the same proof can be used for a quasistationary model for the chemoattractant, i.e., when the time derivative is cancelled in the  $s$ -equation. Instead of the result for parabolic equations from [16] a corresponding result from potential theory would have to be used. Since we work in whole space the assumption  $\beta > 0$  on the decay of the chemoattractant helps, but is possibly not essential.*

**Proof:** Local existence is a standard result, and global existence will be a consequence of the estimates we shall derive.

By the assumptions on the initial data and mass conservation we have  $\|u\|_1 = \|u_I\|_1$ . This implies (analogously to Hwang-Kang-Stevens [16]) that  $s$  is bounded in  $W^{1,q}(\mathbb{R}^n)$  uniformly in  $t$ .

The sphere  $S_\rho$  with centre in the origin and radius  $\rho$  is a smooth  $(n-1)$ -dimensional manifold. Therefore, by the standard result on traces,  $W^{1,q}(\mathbb{R}^n)$  is continuously embedded in  $W^{1-1/q,q}(S_\rho)$  and, consequently, also in  $L^1(S_\rho)$  (by the boundedness of  $S_\rho$ ). Therefore,

$$|\overset{\circ}{\nabla}_\rho f(x=0)| \leq c\|f\|_{W^{1,q}(\mathbb{R}^n)}$$

holds. The choice  $f(x) = s(x_0 + x, t)$  and the translation invariance of the  $W^{1,q}(\mathbb{R}^n)$ -norm imply that  $\|\overset{\circ}{\nabla}_\rho s\|_\infty$  is bounded uniformly in time.

Now the proof is completed by an application of the previous lemma.

■

## 4 Steady States

In this section we investigate steady states of the non local chemotaxis model (2). We will show that steady states cannot have spike local maxima and construct approximative plateau steady states.

Steady states of the non local model (2) satisfy the equations

$$\begin{aligned} 0 &= \nabla \cdot (\nabla u - \chi u \overset{\circ}{\nabla}_\rho s) \\ 0 &= D_s \Delta s + \alpha u - \beta s, \end{aligned} \quad (13)$$

#### 4.1 Linear Stability Analysis in 1-D

To compare the stability properties of the model (2) to those of the classical chemotaxis model (1) we perform a linear stability analysis at the homogeneous steady state for the one-dimensional case of (2).

A homogeneous steady state for system (13) is given by  $(\bar{u}, \bar{s})$  where  $\bar{s} = \alpha \bar{u} / \beta$ , and  $\bar{u}$  is determined by the initial population density. Linearization of (2) in 1-D at the steady state gives

$$\begin{aligned} u_t &= u_{xx} - \chi \bar{u} (\overset{\circ}{\nabla}_\rho s)_x \\ s_t &= D_s s_{xx} + \alpha u - \beta s, \end{aligned} \quad (14)$$

We use Fourier transformation to obtain the characteristic equation between eigenvalues  $\lambda$  and modes  $k$ . The 1-D nonlocal gradient is

$$\overset{\circ}{\nabla}_\rho s = \frac{1}{2\rho} (s(x + \rho) - s(x - \rho))$$

while its Fourier transform is given by

$$\mathcal{F}(\overset{\circ}{\nabla}_\rho s) = i \frac{\sin(k\rho)}{\rho} \mathcal{F}(s).$$

Transforming the linearized system (14), we find that the stability is determined by the eigenvalues  $\lambda$  of the matrix

$$A_k := \begin{pmatrix} -k^2 & k\chi\bar{u}\frac{\sin(k\rho)}{\rho} \\ \alpha & -D_s k^2 - \beta \end{pmatrix}.$$

The trace and determinant of  $A_k$  are

$$\text{tr} A_k = -k^2(1 + D_s) - \beta < 0 \quad \det A_k = k^2(D_s k^2 + \beta) - \alpha \chi \bar{u} k \frac{\sin(k\rho)}{\rho}.$$

For  $k = 0$  we find  $\det A_0 = 0$ . Hence, for  $k = 0$  there exists an eigenvalue  $\lambda_0 = 0$ , which relates to the conservation property of (2). For a given total population we obtain instability, if we find a mode  $k > 0$  for which  $\det A_k < 0$ . This translates into the condition

$$k(D_s k^2 + \beta) < \alpha \chi \bar{u} \frac{\sin(k\rho)}{\rho}. \quad (15)$$

Note that for  $\rho \rightarrow 0$ , we have  $\frac{\sin(k\rho)}{\rho} \rightarrow k$ . Then (15) reduces to the necessary condition for pattern formation in the classical chemotaxis model (1), i.e.

$$D_s k^2 + \beta < \alpha \chi \bar{u}. \quad (16)$$

Since for each  $\rho > 0$ ,  $\frac{\sin(k\rho)}{\rho} < k$ , condition (15) for instability in the non-local model is stronger than the corresponding condition (16) for the classical model. In particular, given that (16) is satisfied, it is always possible to determine a bounded  $\rho_c$  for which no pattern formation is possible for  $\rho > \rho_c$ . Since  $|\sin(x)| \leq 1$  we can explicitly calculate

$$\rho_c = \sup_{k>0} \left\{ \frac{\alpha \chi \bar{u}}{k(D_s k^2 + \beta)} \right\}.$$

For example, if we study (2) with homogeneous Dirichlet boundary conditions on an interval  $[0, L]$ , then the supremum would be obtained for  $k = \pi/L$ .

## 4.2 Properties of the Non-Local Gradient

The nonlocal gradient (3) has the properties that  $\overset{\circ}{\nabla}_\rho s(x, t) = 0$  for constant distribution  $s$  and that for differentiable  $s(x)$  we have

$$\lim_{\rho \rightarrow 0} \overset{\circ}{\nabla}_\rho s(x) = \nabla s(x).$$

It is rather useful to study the Taylor expansion of the non local gradient for small  $\rho > 0$ . In Hillen [9] it is shown that

$$\overset{\circ}{\nabla}_\rho s(x) = \nabla s(x) + \frac{\rho^2}{2(2+n)} \nabla(\Delta s(x)) + \mathcal{O}(\rho^4), \quad (17)$$

where  $n$  is the space dimension and  $\Delta$  denotes, as usual, the Laplacian. Hence the first correction term to  $\nabla s$  is of third order.

We replace  $\nabla s$  in the classical chemotaxis model (1) by the nonlocal gradient  $\overset{\circ}{\nabla}_\rho s$  and obtain the nonlocal chemotaxis model (2).

As shown in [9] the nonlocal gradient can be used to classify local maxima and to distinguish spikes versus plateaus.

**Definition 4.1** (from [9]) *A local maximum  $x_0$  of  $f : U \subset \mathbb{R}^n \rightarrow \mathbb{R}$  is called a*

$$\begin{aligned} \text{spike} \quad &\Longleftrightarrow \quad \exists \rho^* > 0 \quad \text{such that} \\ &\quad \mathring{\nabla}_\rho (\nabla f(x_0)) - \text{Hess}(f(x_0)) \quad \text{is positive} \\ &\quad \text{definite for all } 0 < \rho < \rho^*, \end{aligned}$$

$$\begin{aligned} \text{plateau} \quad &\Longleftrightarrow \quad \exists \rho^* > 0 \quad \text{such that} \\ &\quad \mathring{\nabla}_\rho (\nabla f(x_0)) - \text{Hess}(f(x_0)) \quad \text{is negative} \\ &\quad \text{definite for all } 0 < \rho < \rho^*. \end{aligned}$$

Using the  $n$ -dimensional Taylor expansion we have proven in [9]

**Theorem 4.1** *Assume  $f \in C^5(U)$  and  $\text{Hess}(\Delta f(x_0))$  is invertible. Then*

$$x_0 \quad \text{is a spike} \quad \Longleftrightarrow \quad \text{Hess}(\Delta f(x_0)) \quad \text{is positive definite,}$$

$$x_0 \quad \text{is a plateau} \quad \Longleftrightarrow \quad \text{Hess}(\Delta f(x_0)) \quad \text{is negative definite.}$$

### 4.3 No Spikes

**Theorem 4.2** *Assume the steady state  $u(x), s(x)$  of (2) have a common local maximum. Then this maximum cannot be a spike.*

**Proof.** We rewrite the first equation of (13) as

$$0 = \nabla \cdot (\nabla u - \chi u \nabla s + \chi u (\nabla s - \mathring{\nabla}_\rho s))$$

and introduce

$$\psi = u e^{-\chi s}.$$

Then we obtain

$$\begin{aligned} 0 &= \nabla \cdot (\nabla \psi e^{\chi s}) + \chi \nabla \cdot (u (\nabla s - \mathring{\nabla}_\rho s)) \\ &= e^{\chi s} \left( \Delta \psi + \chi \nabla \psi \cdot (2 \nabla s - \mathring{\nabla}_\rho s) \right. \\ &\quad \left. + \chi \psi (\nabla s \cdot (\nabla s - \mathring{\nabla}_\rho s) + \nabla \cdot (\nabla s - \mathring{\nabla}_\rho s)) \right) \end{aligned} \quad (18)$$

Now we assume that  $u, s$  and  $\psi$  have a common local maximum at  $x_0 \in M$ , i.e.

$$\nabla \psi(x_0) = 0, \quad \Delta \psi(x_0) < 0, \quad \nabla u(x_0) = 0, \quad \Delta u(x_0) < 0, \quad \nabla s(x_0) = 0, \quad \Delta s(x_0) < 0.$$

Then (18) reduces to

$$0 = \Delta\psi + \chi\psi(\Delta s - \nabla \cdot \overset{\circ}{\nabla}_\rho s). \quad (19)$$

If the local maximum is a spike as defined in Definition 4.1, then the matrix

$$\overset{\circ}{\nabla}_\rho (\nabla s(x_0)) - \text{Hess}(s(x_0))$$

is positive definite. This implies in particular that

$$\Delta s(x_0) - \nabla \cdot \overset{\circ}{\nabla}_\rho s(x_0) < 0,$$

which together with  $\Delta\psi(x_0) < 0$  gives a contradiction to (19). Hence  $x_0$  cannot be a spike.

#### 4.4 Approximate Plateaus

We saw in the previous subsection that steady state solutions are not of spike type. Here we show that pattern formation still can occur in form of plateau solutions. We were not successful to explicitly find plateau solutions for the nonlocal model (13), we can, however, find approximate steady states.

For  $\rho$  small enough the nonlocal gradient can be approximated as shown in (17). We take the first two terms and define

$$\phi(x) := s + \frac{\rho^2}{2(2+n)} \Delta s$$

Then the approximate steady states on a smooth bounded domain  $\Omega$  satisfy the fourth order equation

$$\begin{aligned} 0 &= \nabla \cdot (\nabla u - \chi u \nabla \phi) \\ 0 &= D_s \Delta s + \alpha u - \beta s, \end{aligned} \quad (20)$$

From this representation we see that the nonlocal gradient regularizes the same way as a fourth order term does. System (20) has a similar structure as the classical PKS model (1), which was studied by Nanjundiah [22]. We use the same transformation here:

$$\Psi = ue^{-\chi\phi}$$

and obtain

$$0 = (\Delta\Psi + \chi\nabla\Psi \cdot \nabla\phi)e^{\chi\phi}.$$



Hence  $\Psi$  satisfies a Hopf maximum principle, thus  $\Psi(x)$  must be constant.

$$\Psi(x) = \Psi.$$

Since  $\Psi = ue^{-\chi\phi}$  we find

$$u = \Psi e^{\chi\phi} \quad \phi = \frac{1}{\chi}(\ln u - c), \quad c = \ln \Psi.$$

The steady state system (20) becomes

$$\begin{aligned} s + \frac{\rho^2}{2(2+n)}\Delta s &= \frac{1}{\chi}(\ln u - c) \\ D_s \Delta s &= \beta s - \alpha u, \end{aligned} \tag{21}$$

We use the second equation of (21) to replace  $\Delta s$  in the first equation, which gives

$$\begin{aligned} s \left( 1 + \frac{\beta\rho^2}{2(2+n)D} \right) &= \frac{\alpha\rho^2}{2(2+n)D}u + \frac{1}{\chi}(\ln u - c) \\ D_s \Delta s &= \beta s - \alpha u, \end{aligned} \tag{22}$$

For convenience we introduce

$$\kappa := \frac{\rho^2\chi}{2(2+n)D}$$

and we solve the first equation of (22) for  $s$ :

$$s = \frac{\alpha\kappa u + \ln u - c}{\chi + \beta\kappa}$$

This expression for  $s$  is then used in the second equation of (21) to obtain a second order equation for  $u$ :

$$\Delta u \left( \alpha\kappa + \frac{1}{u} \right) - \frac{(\nabla u)^2}{u^2} = \frac{\beta}{D} \ln u - \frac{c}{D} - \frac{\alpha\kappa}{D}u. \tag{23}$$

We study the one-dimensional case on an interval  $[0, l]$  with homogeneous Neumann boundary conditions in more detail. In one space dimension equation (23) can be written as a first order system

$$\begin{aligned} u' &= w \\ w' &= \frac{Dw^2 + \beta u^2 \ln u - cu^2 - \alpha\chi u^3}{D(\alpha\chi u^2 + u)} \end{aligned} \tag{24}$$

with boundary conditions

$$w(0) = 0 \quad w(l) = 0.$$

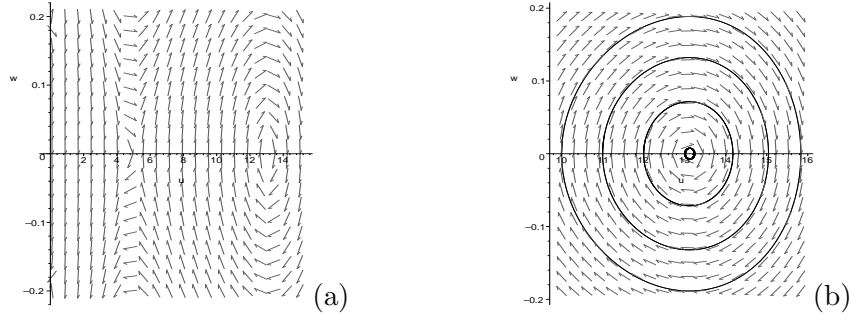


Figure 1: (a) The vectorfield for the case of three roots of the equation (25). (b) Plateaus solutions appear as closed circles around the third equilibrium point.

The steady states of (24) satisfy  $w = 0$  and  $u = 0$  or

$$\beta \ln u - c - \alpha \chi u = 0. \quad (25)$$

The equation (25) has zero, one or two roots. In a systematic analysis of all cases (not shown here) it turns out that only the case of three roots gives non-trivial steady states. In Figure 1 we show an example for  $D = 1, \mu = 0.12, \beta = 1, \nu = 1, \kappa = 10$ . In Figure 1 (a) the vectorfield of (24) is shown and in Figure 1 (b) typical nontrivial plateau steady states are shown in the phase plane.

Note that for  $\rho \rightarrow 0$  equation (25) becomes  $\beta \ln u = c$ , hence it has exactly one root at  $u = \psi e^{\beta}$ . The third root diverges to  $\infty$  and the plateau steady states disappear.

## 5 Numerical Results

### 5.1 Numerical Method

We turn our attention to numerical solutions of the non-local chemotaxis model. The right-hand sides of the system (2) are discretised in conservative flux form, employing a second order central differencing scheme for the diffusion terms and a high order upwinding method with a Koren flux limiting function for the advective term. The conservative flux form is appropriate for the diffusion-advection equation, as it ensures mass conservation ([15, 18]). Flux limiting allows higher order upwinding for the advective term while maintaining positivity of solutions. This has previously been employed to solve standard chemotactic type systems (e.g. [38]). The direction

for the upwinding will depend on the sign of the non-local term in the advective component, calculated at the boundary between adjacent mesh points. In one dimension, it is thus necessary to calculate concentration data at  $c(x_b \pm \rho)$ , where  $x_b$  denotes the midpoint between adjacent mesh points. We approximate  $c(x_b \pm \rho)$  by linear interpolation using the nearest two mesh points. The two-dimensional problem is solved analogously, yet determining the non-local term now requires calculation of the integral on a circle of radius  $\rho$ , centred on the mid-point between adjacent mesh points. We approximate this by discretising the surface into a lattice of surface grid points, and employing linear interpolation from the surrounding domain grid points to give cell/chemical densities at the surface, see Figure 2 (a). Time integration is carried out using an explicit trapezoidal scheme; investigations into higher order schemes (e.g. 4th order Runge-Kutta) yielded little difference. More efficient time integration techniques, for example applying “operator-splitting” and using distinct methods (e.g. implicit, explicit) to each right hand side term would be required for more extensive numerical studies.

For simplicity in calculating the non-local terms, we set periodic boundary conditions; biologically relevant boundary conditions (e.g. Dirichlet or zero-flux) can also be applied, yet one must pay appropriate attention to the non-local term near the boundaries. To determine the accuracy of the solver, a series of test simulations are performed. Since an explicit solution is unknown, an “accurate” reference solution is obtained at time  $T$ ,  $U_{ref}(\mathbf{x}, T)$  by solving the equations on a highly refined grid. For the small time steps necessary in implementing the explicit trapezoidal rule, temporal errors become negligible and can safely be ignored. Solutions are obtained for different grid steps  $h$  to obtain  $U_h(\mathbf{x}, T)$ , and we determine the error by calculating the discrete  $L_1$  norm,

$$\|E_h\|_1 = \sum_i h^n |U_h(x_i, T) - U_{ref}(x_i, T)|$$

where  $n$  is the dimension. Plots of  $h$  vs  $\|E\|_1$  are shown for  $n = 1$  in Figure 2 (b) and  $n = 2$  in Figure 2 (c). Errors are shown for two methods of solving the advective term, the high order scheme with flux limiting and a simple first order scheme. The latter requires a large number of grid points to achieve comparable accuracy to the high order scheme. The numerical order of accuracy for the high order scheme can be determined as approximately 2, in line with previous results, e.g. [15]. The results from other numerical tests are comparable.

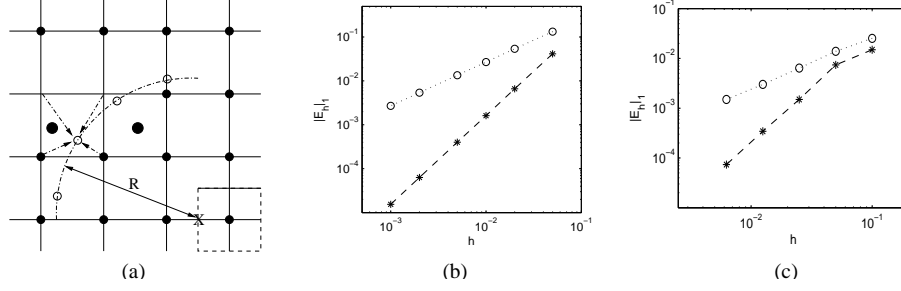


Figure 2: (a) To calculate the integral at the point  $X$ , we discretise the surface into regularly spaced lattice points (white circles). The chemical concentrations/cell densities at each white circle necessary for calculating the integral are determined through interpolation of the surrounding domain lattice points (black circles). (b)  $\|E\|_1$  errors for the 1D numerical scheme. For this we solve the model equations in 1D with the following parameters:  $D_u = D_v = \alpha = \beta = 0.01$ ,  $\chi = 0.05$  and  $\rho = 0.1$  on the domain  $[0, 1]$  with periodic BCs. ICs are  $u(x, 0) = 1.0$  and  $v(x, 0) = 0.5 + 1.0e^{-(x-0.5)^2}$ . For the reference solution we use a mesh with grid step  $h = 1/5000$ . The time step is  $10^{-6}$  and we compare solutions at  $t = 5$ . (c)  $\|E\|_1$  errors for the 2D numerical scheme. Parameters as in (b) except  $\chi = 0.04$  and  $\rho = 0.05$  on the domain  $[0, 1] \times [0, 1]$ . We use a reference solution with grid step  $h = 1/500$  and compare solutions at  $t = 0.2$ .

## 5.2 Aggregation Results

### 5.2.1 1D Numerics

In Figure 3 we show the results of a typical simulation of the 1D non-local model. Parameters have been selected such that the instability condition, (15), is satisfied. The numerics demonstrate the formation of multiple cell aggregations, which subsequently undergo a coarsening process until a single peak remains. This behaviour is analogous to that observed in Keller-Segel type models of chemotaxis (e.g. see [28]).

To demonstrate the effect of the sampling radius, we simulate the model over a range of  $\rho$ . For  $\rho \rightarrow 0$ , the non-local model reduces to the classical Keller-Segel model (1) and we plot solutions for this case in Figure 4 (a) for comparison. Numerical simulations at small  $\rho$ , Figure 4 (b) demonstrate a predictably close match. Increasing the radius results in a lower peak/broader aggregation, (c)-(f). It is possible to use condition (15) to

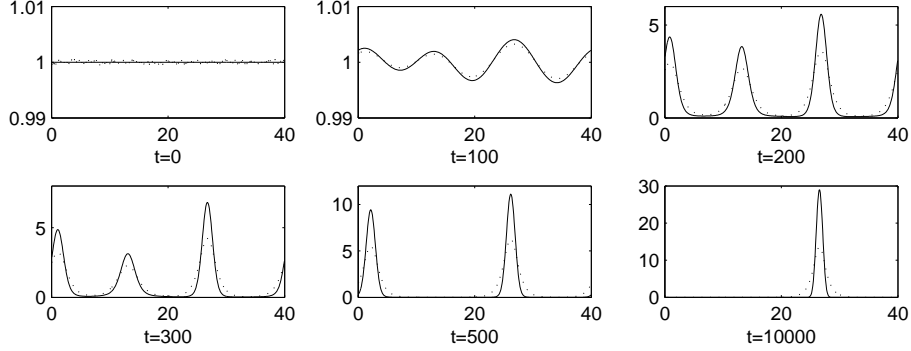


Figure 3: Evolving cell (solid) and chemical (dotted) profiles for the 1D non-local model. The following parameters are chosen:  $D_u = D_s = \alpha = \beta = 1.0$ ,  $\rho = \chi = 2.0$  on a domain  $[0, 40]$  with periodic boundary conditions. We initially set  $u(x, 0) = 1.0$  and a small random perturbation of the homogeneous steady state for the chemical concentration. 401 mesh points are used for the grid.

determine the critical value for  $\rho$  above which patterning is no longer possible. The lowest non-zero mode  $k$  satisfying the boundary conditions is  $k = 2\pi/L$ , where  $L$  is the domain length. Substituting this, together with the parameters listed in Figure 4, into (15) we determine  $\rho_c = 2.2552$  to 4 d.p. This value is both confirmed by and validates the accuracy of the numerical simulations: for  $\rho_c = 2.255$  an aggregation (albeit small) eventually develops, Figure 4 (g), while an increase of  $\rho_c$  to 2.256 results in no pattern formation, (h).

### 5.2.2 2D Numerics

We extend the numerical analysis to two dimensions. In 2D the classical Keller-Segel model is known to exhibit finite time blow-up (for suitable initial data). A typical scenario is shown in Figure 5 (a): already at  $T = 13.8$  the cell density is highly concentrated, and the solution can no longer be computed (numerical blow-up). In Figures 5 (b)-(e) we plot cell density profiles under different  $\rho$  for the non-local model. The global existence result for the non-local model is confirmed by the numerics: inclusion of a sampling radius prevents blow-up and allows solutions to evolve to a heterogeneous steady state solution. The 2D numerics parallel the 1D observations: decreasing  $\rho$  results in a concentrated solution and a plot of the maximum

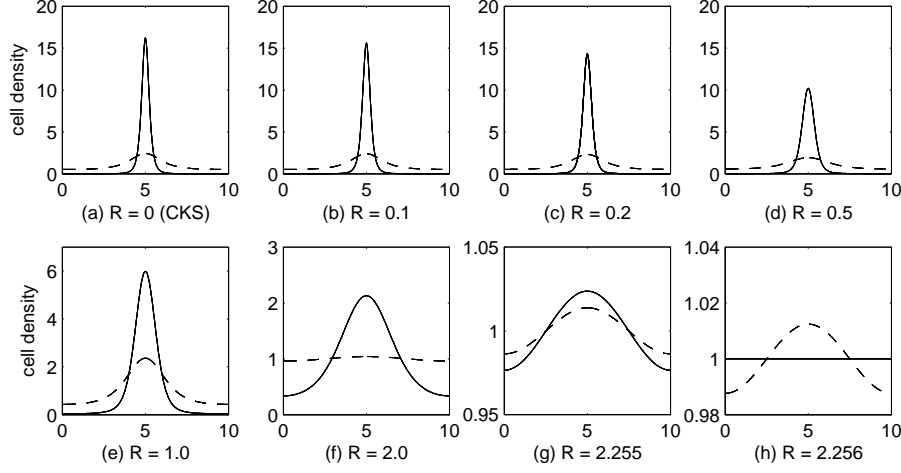


Figure 4: Intermediate (dashed) and long term (solid) cell density profiles for the non-local model under various  $\rho$ : (a)  $\rho = 0$ , corresponding to the classical Keller-Segel model, at times  $T = 30$  and  $200$ ; (b)  $\rho = 0.1$  at  $T = 30, 200$ ; (c)  $\rho = 0.2$  at  $T = 30, 200$ ; (d)  $\rho = 0.5$  at  $T = 30, 200$ ; (e)  $\rho = 1.0$  at  $T = 40, 500$ ; (f)  $\rho = 2.0$  at  $T = 40, 500$ ; (g)  $\rho = 2.255$  at  $T = 1000, 200000$ ; (h)  $\rho = 2.255$  at  $T = 1000, 200000$ . Parameter values as for Figure 3 on a domain  $[0, 10]$  (201 mesh points). Initial conditions are  $u(x, 0) = 1.0$ ,  $v(x, 0) = 0.95 + 0.1 \exp(-0.1(x - 5)^2)$ .

density vs  $\rho$  appears consistent with convergence to a blow-up solution as  $\rho \rightarrow 0$ , Figure 5 (f). Increasing  $\rho$  results in a dispersed peak and above some critical radius  $\rho_c$  aggregation is no longer possible Figure 5 (e) .

In Figure 6 we plot solutions on a larger initial domain; here initial conditions consist of a random spatial perturbation from the homogeneous steady state. Simulations indicate pattern formation, with a number of cell aggregations emerge at (roughly) equally spaced locations. Altering the sampling radius alters both the density of the peak, but also the number of the aggregations to emerge.

### 5.3 Model Variations

Numerical investigations above have been limited to the system (2) with (3). The numerical results confirm the earlier analysis: critically, we observe global existence for the non-local model. However, forms for the nonlocal

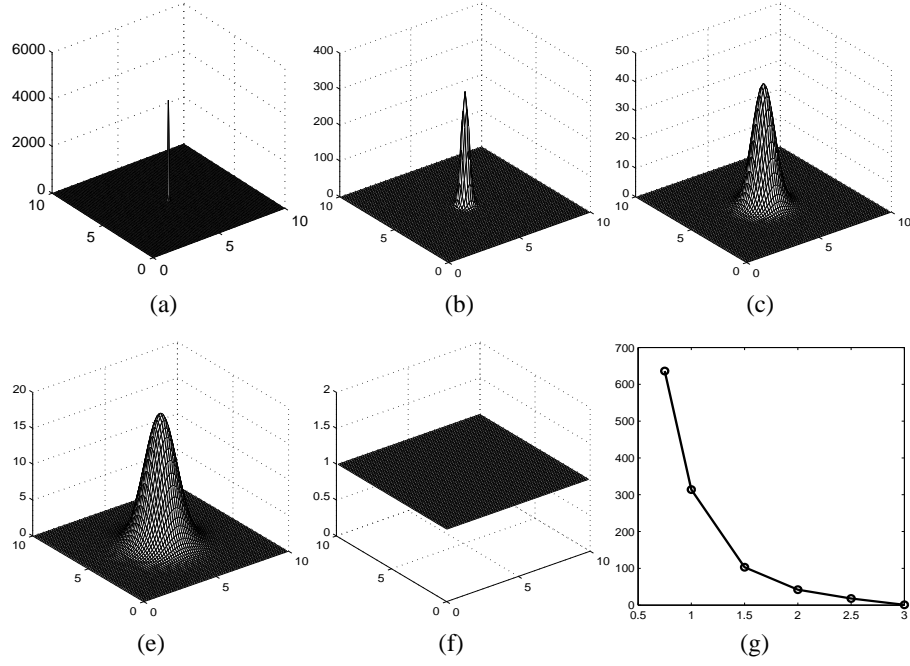


Figure 5: (a) Numerical simulation of the classical Keller-Segel model ( $\rho = 0$ ). Simulation shown at  $t = 13.8$ , just prior to “numerical blow-up”. (b)-(e) Steady state cell density patterns for the non-local model for increasing  $\rho$ : (b)  $\rho = 1.0$ ,  $T = 100$  (c)  $\rho = 2.0$ ,  $T = 150$  (d)  $\rho = 2.5$ ,  $T = 300$ , (e)  $\rho = 3.0$ ,  $T = 300$ . (f) Plot showing peak cell density as a function of  $\rho$ . Model parameters as for Figure 3 on the domain  $[0, 10] \times [0, 10]$  (75 by 75 grid points used). Initial conditions are  $u(x, y, 0) = 1.0$  and  $s(x, y, 0) = 0.5 + e^{-0.5((x-5)^2 + (y-5)^2)}$  on the domain  $[0, 10] \times [0, 10]$ .

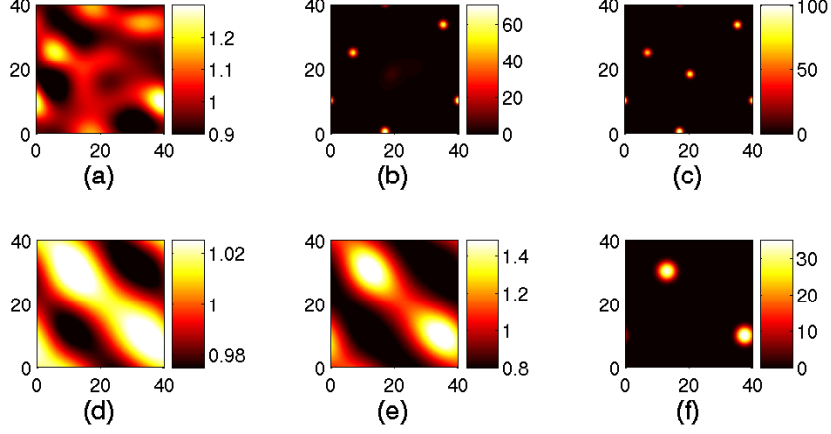


Figure 6: Top row: cell density evolution for  $\rho = 3.0$  for (a)  $t = 100$ , (b)  $t = 150$  (c)  $t = 200$ . Bottom row: cell density evolution for  $\rho = 6.0$  for (d)  $t = 200$ , (e)  $t = 300$  (f)  $t = 400$ . Parameters as for 3 on the domain  $[0, 40] \times [0, 40]$  ( $100 \times 100$  mesh points). Initially we take  $n(x, y, 0) = 1$  and a random perturbation about the homogeneous chemical concentration.

term other than (3) are clearly valid, as indicated in the derivations. Here we consider the implications of different choices for the non-local term.

### 5.3.1 Dependence on the Sampling Radius

Different  $\rho$ -scalings of the non-local term can have a large impact on the dependence of solutions on  $\rho$ . In the above simulations, the non-local term (3) features a scaling by  $\frac{n}{\omega\rho}$ . While this allows direct comparison with the classical model, it can perhaps be criticised on other grounds. The linear stability analysis of Section 4.1 demonstrates an upper bound on the sampling radius for a patterning instability to occur. The existence of this upper bound is intuitive: above a certain radius, the size of the sampling region will be so large that any spatial variations are lost. However, in (15) there is no *lower bound* on the sampling radius for a patterning instability. In reality, it is believed only larger cells can *spatially* resolve a gradient; smaller organisms such as *E. coli* must employ temporal sensing to expand their sampling radius. It may therefore be more reasonable to expect a minimum sampling radius for pattern formation, below which cells are unable to



resolve a spatial gradient, and hence aggregate.

This behaviour can be incorporated into the model with different  $\rho$  scalings of the non-local term 3. For example, suppose we replace the  $\frac{n}{\omega\rho}$  with  $\frac{1}{\omega}$  (or 1 in 1-D) in Equation (3): this corresponds to a scaling of 1/membrane surface area rather than 1/cell volume. A 1D linear stability analysis along the lines of Section 4.1 predicts an alternative instability condition to (15)

$$\sin(k\rho) > \frac{k^2(D_s k^2 + \beta)}{2\chi\alpha\bar{u}k}.$$

For non-zero  $k$  the above now determines a critical radius  $\rho_c$ , below which pattern formation is not possible; using the parameters of the simulations in Figure 7, and choosing the minimum non-zero  $k$  (corresponding to a single peak solution) we find  $\rho_c = 0.275$ . This value is confirmed in the numerical simulations of Figure 7. For  $\rho < \rho_c$ , Fig 7(a), no aggregations develop while  $\rho > \rho_c$  gives rise to pattern formation, Fig 7(b)-(c). The behaviour is also observed in 2D Fig 7(d)-(f).

### 5.3.2 Incorporation of Receptor Binding

During the derivations of the model, linear functions have been chosen to describe key processes for simplicity. More plausible, nonlinear forms, can also be chosen; for example by taking a saturating dependence on the signal concentration (i.e. of the form (5) in (4) or in (6)), we derive the following non-local term:

$$\int_{S^{n-1}} \sigma \frac{s(x + R\sigma, t)}{k + s(x + R\sigma, t)} d\sigma.$$

Replacing the integral term in equation 3 with the above still allows pattern formation, albeit with a less concentrated peak, Figure 8 (a).

### 5.3.3 Non-Diffusing Scenarios

Tactic responses to non-diffusing substances can occur in a number of instances. ‘‘Haptotaxis’’, for example, describes cell movement along gradients of adhesion molecules tightly bound to a rigid extracellular matrix. Non-diffusing chemical species for classical chemotaxis models can create greater numerical challenges; steeper gradients occur and blow-ups develop even in 1D. Numerics indicate that the finite-sampling method resolves these difficulties and solutions still appear to exist globally, Figure 8 (b).

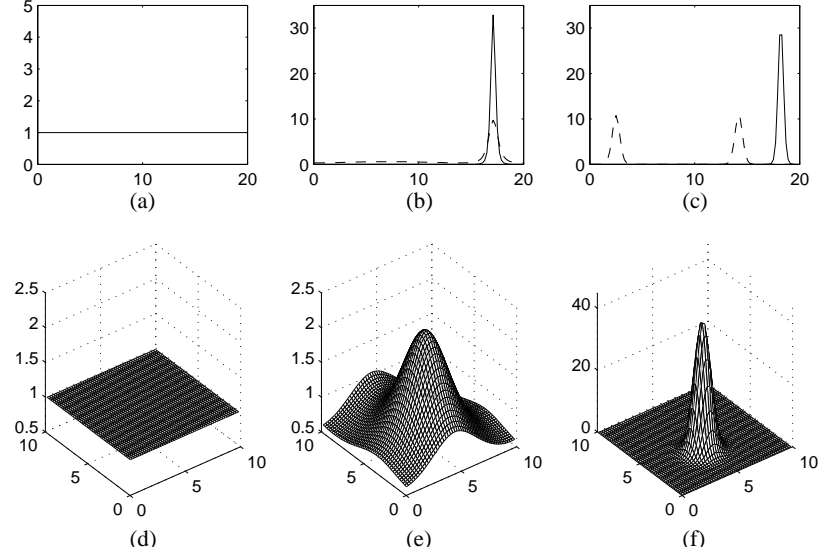


Figure 7: (a)-(c) 1D cell densities for an alternative  $\rho$ -scaling of the non-local term: (a)  $\rho = 0.25$ ; (b)  $\rho = 0.3$  at  $t = 1000$  (dashed) and  $t = 3000$  (solid); (c)  $\rho = 1.0$  at  $t = 500$  (dashed) and  $t = 3000$  (solid). At larger  $R$ , multiple peaks emerge initially and subsequently coalesce into a single aggregation. (d)-(f) 2D cell density patterns: (d)  $\rho = 1.0$  at  $t = 200$ ; (e)-(f)  $\rho = 2.0$  at times  $t = 100$  and  $t = 200$  respectively. For both 1&2D numerics we use the parameters of Figure 5 on the domains  $[0, 20]$  (1D) and  $[0, 10] \times [0, 10]$  (2D). Initial conditions are  $u(x, 0) = 1$  and a random perturbation around the homogeneous chemical steady state.

## 6 Discussion

In this paper we introduced a non-local gradient sensing term into the classical chemotaxis equations. We have proven that solutions to the non local model exist globally in time, independent of the space dimension. We have seen that, as  $\rho \rightarrow 0$ , the solutions become higher and steeper and finally blow-up for  $\rho = 0$ . In addition, plateau steady states cease to exist for  $\rho = 0$ .

In the introduction we mentioned three alternative regularizations to the non-local sensing that also prevent blow-up: (i) saturation, (ii) volume filling, and (iii) attraction-repulsion. In reality, all four mechanisms may be operation and thus we summarize the results for each of these regulariza-

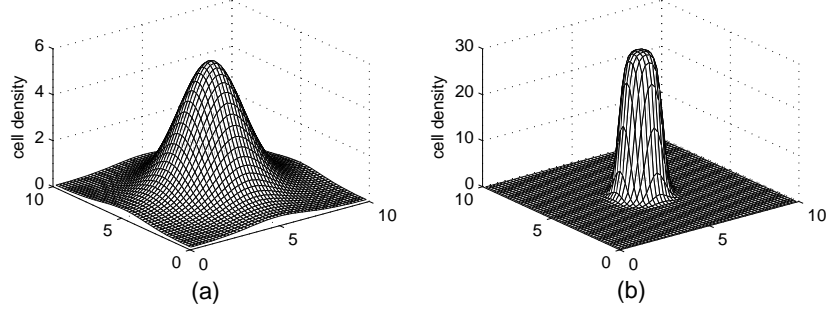
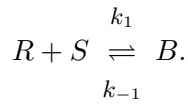


Figure 8: Asymptotic cell density for two model variations: (a) “receptor-binding” non-local term; (b) non-diffusion of the chemical species. Model parameters and initial conditions as for Figure 3 except in (a) where  $\chi = 8$  and  $k = 1$  and (b) where  $D_s = 0$ . Simulations solved on a domain  $[0, 10] \times [0, 10]$  with 51 by 51 grid points.

tions,

### 6.1 Saturation Effects

If we assume the signal  $s$  binds to certain cell surface receptors, for high levels of  $s$  all receptors may be occupied and the cell is unable to detect a gradient. Following the argument of Othmer and Stevens [27], we let  $S$  denote the chemical signal,  $R$  a free cell surface receptor and  $B$  an occupied one, and



If this is fast, the quasi steady-state will be  $b = \frac{Ks}{s+\gamma}$ , with equilibrium constant  $\gamma = \frac{k_{-1}}{k_1}$ , and lower case letters denoting concentrations. Assuming cells base their movement on a local gradient of the number of bound receptors, we derive a non-linear chemotactic form,  $\chi(s)$  (e.g. see [27]), where

$$\chi(s) \sim \frac{K\gamma}{(\gamma + s)^2},$$

and the classical chemotaxis model (1) is modified to

$$\begin{aligned} u_t &= \nabla \cdot (\nabla u - u\chi(s)\nabla s) \\ s_t &= D_s \Delta s + \alpha u - \beta s. \end{aligned} \quad (26)$$

The above  $\chi(s)$ , and other forms, are commonly used in applications. Segel and Jackson [37] assume a Weber-Fechner response law  $\chi(s) = \frac{c_1}{s}$ . Rivero *et al.* [36] replace the whole expression  $\chi(s)s_x$  by

$$\chi(s)s_x \sim \tanh\left(\frac{c_1 s_x}{c_2 + s^2}\right).$$

Ford and Lauffenburger [8] and also Tyson, Lubkin and Murray [38] assume the receptor kinetic model from above:  $\chi(s) = \frac{c_1}{c_2 + s^2}$ , which was generalised by Levine and Sleeman [19] to  $\chi(s) = \frac{a(\gamma-\beta)}{(s+\gamma)(s+\beta)}$ . Höfer, Sherrat and Maini [13] assume  $\chi(s) = \frac{\chi_0 s^m}{A^m + s^m}$ .

Biler [3] studied saturation effects in chemotaxis models from a theoretical point of view. He introduced a *chemotactic potential*,  $\phi$ , which is given as the integral of  $\chi$ :

$$\chi(s)\nabla s = \nabla\phi(s).$$

The potential is defined to be *strictly sublinear*, if

$$\chi(s) > 0, \quad \chi(s) \rightarrow 0, \text{ as } s \rightarrow \infty, \quad \chi(s)s \text{ is increasing.}$$

Then Biler shows the following result [3]:

**Theorem 6.1** *If  $n = 2$  and  $\phi(s)$  is strictly sublinear the solution to (26) exist globally in time. Moreover, if  $n \leq 2$  and  $\chi(v) = \chi_0/v$  with  $\chi_0 < 2/n$  then the solutions of (26) exist globally in time.*

## 6.2 Volume Filling

Hillen and Painter [11, 28] introduced mechanistic descriptions of volume effects. It is assumed that cells have a certain finite (nonzero) volume and the occupation of an area by cells limits other cells from penetrating it. This effect was modelled by introducing a function  $q(u)$  describing the probability of finding space for a local cell density  $u$ . A typical example is  $q(u) = 1 - u/U_{\max}$ , for  $0 \leq u \leq U_{\max}$ , where  $U_{\max}$  denotes a maximum cell density. The volume filling model reads (see [28])

$$\begin{aligned} u_t &= \nabla \cdot (D(q(u) - q'(u)u)\nabla u - \chi u q(u)\nabla s) \\ s_t &= D_s \Delta s + \alpha u - \beta s. \end{aligned} \quad (27)$$

The qualitative properties of the volume filling model is quite well understood. Global existence of solutions in any space dimension has been shown in [11] for special cases and in Wrzosek [41] for the full model (27). Also, Wrzosek [41] showed the existence of a compact global attractor. The structure of the attractor can be understood using Lyapunov functions [42]. In [28] it was shown numerically that typical patterns are of plateau type with long transient times. In Potapov and Hillen [33] the metastability of steady states was studied and the underlying bifurcation diagram was identified. The leading unstable eigenvalues are exponentially small. In Dolak and Schmeiser [6] the plateau interactions were studied using asymptotic methods. Dolak and Schmeiser are able to obtain a system of ODE's for the location of transition layers. Finally, in Dolak and Hillen [5], the volume filling idea has been used to model pattern formation of *Dictyostelium discoideum* and *Salmonella typhimurium*.

### 6.3 Attraction-Repulsion Mechanisms

Many motile cells demonstrate both chemoattraction and chemorepulsion, depending on the environmental signal; for example *E. coli* bacteria demonstrate attraction to sugars and amino acids and repulsion from noxious substances. Incorporating these competing factors into the classical chemotaxis model results in the following model

$$\begin{aligned} u_t &= \nabla \cdot (\nabla u - \chi_a u \nabla a + \chi_r u \nabla r) \\ a_t &= D_a \Delta a + g(u, a, r) \\ r_t &= D_r \Delta r + h(u, a, r). \end{aligned} \tag{28}$$

Models of the above type have been examined by a number of authors (e.g. [29, 20, 28]). In [28] the authors examined a specific form of the above equation in which  $g(u, a, r) = \alpha_a u - \beta_a a$  and  $h(u, a, r) = \alpha_r u a - \beta_r r$ . An interpretation for this model would be secretion of both an internally produced chemoattractant and a chemorepellent signal; for example a toxic substance produced as a byproduct of the internal biochemical pathways involved in chemotaxis/synthesis. The qualitative properties of (28) are currently under investigation. In Renclawowicz and Hillen [35], it is shown that there are special cases of (28) that have global in time solutions, whereas other special cases show finite time blow-up solutions. A general theory for (28) still needs to be developed.

## 6.4 Future Work

The explicit incorporation of a non-local sampling radius for the cell response to its environment provides a new level of detail for describing cell migration in response to external cues. In this paper, we have explored the general property of solutions to the model including its ability to exhibit pattern formation, the global existence of solutions and the nature of the steady states.

Numerical simulations of the model indicated the global existence properties of the non-local model may extend to even stronger cases than that determined theoretically in Section 3. For example under zero-diffusion of the chemical species, a case that leads to blow-up even in 1D for the classical chemotaxis model, steady state patterns still develop (Figure 8 (b)). This result remains to be demonstrated analytically.

While this paper has not had a specific biological application in mind, it is necessary to consider the use of the model in specific biological processes. The explicit incorporation of a non-local sampling radius, with its length scale of cell diameters, limits the ability to perform numerical explorations at “truly macroscopic scales” (for example, the size of large tissues/organs or *Dictyostelium* and bacteria aggrgations). Thus, this model may be most appropriate at a “mesoscopic-level” - i.e. where the length scales of movement are not “hugely” greater than the size of individual cells, but when a macroscopic approach is still desirable. Two such applications include the formation of vascular patterns, or the invasion of tumour cells into surrounding tissue. An open question is thus raised as to whether it is possible to derive fully macroscopic models (i.e. PDE models) which retain the important characteristics of the non-local sampling radius. A clue to one approach for this may lie in the Taylor Expansion of the non-local term, Equation (17). While applying the first non-zero term in this expansion leads straight to the classical Keller-Segel model, using the first two non-zero terms adds a fourth order dissipative term.

## References

- [1] Markowich P. Arnold, A. and G. Toscani. On large time asymptotics for drift-diffusion-poisson systems. *Transport Theory Statist. Phys.*, 29:571–581, 2000.
- [2] H.C. Berg and E.M. Purcell. Physics of chemoreception. *Biophys. J.*, 20(2):193–219, 1977.

- [3] P. Biler. Global solutions to some parabolic-elliptic systems of chemotaxis. *Adv. Math. Sci. Appl.*, 9(1):347–359, 1999.
- [4] Markowich P.A. Perthame B. Chalub, F. and C. Schmeiser. Kinetic models for chemotaxis and their drift-diffusion limits. *Monatsh. Math.*, 142:123–141, 2004.
- [5] Y. Dolak and T. Hillen. Cattaneo models for chemotaxis, numerical solution and pattern formation. *J. Math. Biol.*, 46(2):153–170, 2003.
- [6] Y. Dolak and C. Schmeiser. The keller-segel model with logistic sensitivity function and small diffusivity. *SIAM J. Appl. Math.*, 2005.
- [7] J. Dolbeault and B. Perthame. Optimal critical mass in the two-dimensional keller-segel model in  $\mathbb{R}^2$ . *C. R. Math. Acad. Sci. Paris*, 339:611–616, 2004.
- [8] R.M. Ford and D.A. Lauffenburger. Measurement of bacterial random motility and chemotaxis coefficients: II. application of single cell based mathematical model. *Biotechnol. Bioeng.*, 37:661–672, 1991.
- [9] T. Hillen. A classification of spikes and plateaus. *SIAM Reviews*, 2005. submitted.
- [10] T. Hillen and H.G. Othmer. The diffusion limit of transport equations derived from velocity jump processes. *SIAM J. Appl. Math.*, 61(3):751–775, 2000.
- [11] T. Hillen and K. Painter. Global existence for a parabolic chemotaxis model with prevention of overcrowding. *Adv. Appl. Math.*, 26:280–301, 2001.
- [12] T. Hillen and A. Potapov. Global existence for the classical chemotaxis model in  $1 - D$ . *Math. Meth. Appl. Sci.*, 27:1783–1801, 2004.
- [13] T. Höfer, J.A. Sherratt, and P.K. Maini. *Dictyostelium discoideum* cellular self organization in an excitable biological medium. *Proc. R. Soc. London, B*, pages 249–257, 1995.
- [14] D. Horstmann. From 1970 until present: The Keller-Segel model in chemotaxis and its consequences I. *Jahresberichte der DMV*, 105(3):103–165, 2003.

- [15] W. Hundsdorfer and J.G. Verwer. *Numerical Solution of Time-Dependent Advection-Diffusion-Reaction Equations*, volume 33 of *Springer Series in Computational Mathematics*. Springer-Verlag, Berlin, 2003.
- [16] H.J. Hwang, K. Kang, and A. Stevens. Drift-diffusion limits of kinetic models for chemotaxis: a generalization. *Discrete Contin. Dyn. Syst. Ser. B*, 5:319–334, 2005.
- [17] E.F. Keller and L.A. Segel. Initiation of slime mold aggregation viewed as an instability. *J. Theor. Biology*, 26:399–415, 1970.
- [18] R. J. LeVeque. *Numerical Methods for Conservation Laws*. Lectures in Mathematics. Birkhäuser, Basel, 1992.
- [19] H.A. Levine and B.D. Sleeman. A system of reaction diffusion equations arising in the theory of reinforced random walks. *SIAM J. Appl. Math.*, 57:683–730, 1997.
- [20] M. Luca, A. Chavez-Ross, L. Edelstein-Keshet, and A. Mogilner. Chemotactic signaling, microglia, and Alzheimer’s disease senile plaques: is there a connection? *Bull. Math. Biol.*, 65(4):693–730, 2003.
- [21] M.R. Myerscough, P.K. Maini, and K.J. Painter. Pattern formation in a generalized chemotactic model. *Bull. Math. Biol.*, 60(1):1–26, 1998.
- [22] V. Nanjundiah. Chemotaxis, signal relaying and aggregation morphology. *J. Theoretical Biology*, 42:63–105, 1973.
- [23] J. Nash. Continuity of solutions of parabolic and elliptic equations. *Amer. J. Math.*, 80:931–954, 1958.
- [24] K. Osaki and A. Yagi. Finite dimensional attractor for one-dimensional Keller-Segel equations. *Funkcialaj Ekvacioj*, 44:441–469, 2001.
- [25] H.G. Othmer and T. Hillen. The diffusion limit of transport equations II: Chemotaxis equations. *SIAM J. Appl. Math.*, 62(4):1122–1250, 2002.
- [26] H.G. Othmer and P. Schaap. Oscillatory CAMP signaling in the development of dictyostelium discoideum. *Comments on Theor. Biol.*, 5:175–282, 1998.
- [27] H.G. Othmer and A. Stevens. Aggregation, blowup and collapse: The ABC’s of taxis in reinforced random walks. *SIAM J. Appl. Math.*, 57:1044–1081, 1997.



- [28] K. Painter and T. Hillen. Volume-filling and quorum-sensing in models for chemosensitive movement. *Canadian Appl. Math. Quart.*, 10(4):501–543, 2002.
- [29] K.J. Painter, P.K. Maini, and H.G. Othmer. Complex spatial patterns in a hybrid chemotaxis reaction-diffusion model. *J. Math. Biol.*, 41(4):285–314, 2000.
- [30] K.J. Painter, H.G. Othmer, and P.K. Maini. Stripe formation in juvenile pomacanthus via chemotactic response to a reaction-diffusion mechanism. *Proc. Natl. Acad. Sci. USA*, 96:5549–5554, 1999.
- [31] E.F. Pate and H.G. Othmer. Differentiation, cell sorting and proportion regulation in the slug stage of *Dictyostelium discoideum*. *J. Theor. Biol.*, 118(3):301–319, 1986.
- [32] C.S. Patlak. Random walk with persistence and external bias. *Bull. Math. Biophys.*, 15:311–338, 1953.
- [33] A. Potapov and T. Hillen. Metastability in chemotaxis models. *J. Dynamics Diff. Eq.*, 17, 2005.
- [34] W.J. Rappel, P.J. Thomas, H. Levine, and W.F. Loomis. Establishing direction during chemotaxis in eukaryotic cells. *Biophysical Journal*, 83:1361–1367, 2002.
- [35] J. Renclawowicz and T. Hillen. Analysis of an attraction-repulsion chemotaxis model. *submitted*, 2005.
- [36] M.A. Rivero, R.T. Tranquillo, H.M. Buettner, and D.A. Lauffenburger. Transport models for chemotactic cell populations based on individual cell behavior. *Chem. Eng. Sci.*, 44:1–17, 1989.
- [37] L.A. Segel and J.L. Jackson. Theoretical analysis of chemotactic movement in bacteria. *J. Mechanochem. Cell Motility*, 2:25–34, 1973.
- [38] R. Tyson, S.R. Lubkin, and J.D. Murray. A minimal mechanism for bacterial pattern formation. *Proc. R. Soc. London B*, 266:299–304, 1999.
- [39] B.J. Varnum-Finney, E. Voss, and D.R. Soll. Frequency and orientation of pseudopod formation of *Dictyostelium discoideum* amebae chemotaxing in a spatial gradient: further evidence for a temporal mechanism. *Cell Motil. Cytoskeleton*, 8(1):18–26, 1987.

- [40] C.J. Weijer. Dictyostelium morphogenesis. *Curr. Opin. Genet. Dev.*, 14(4):392–398, 2004.
- [41] D. Wrzosek. Global attractor for a chemotaxis model with prevention of overcrowding. *Nonlinear Analysis*, 59:1293–1310, 2004.
- [42] D. Wrzosek. Long time behaviour of solutions to a chemotaxis model with volume filling effect. *Proc. Roy. Soc. Edinburgh Sect. A*, 2005. to appear.